Analysis of gas-assisted pulverised coal combustion in Cambridge Coal Burner CCB1 using FPV-LES

Journal:	*Energy & Fuels*
Manuscript ID	ef-2020-00317u.R2
Manuscript Type:	Article
Date Submitted by the Author:	n/a
Complete List of Authors:	Chen, Yiran; Tsinghua University, Thermal Engineering Stein, Oliver; University of Stuttgart, Kronenburg, Andreas; University of Stuttgart Xing, Jiangkuan; Zhejiang University State Key Laboratory of Clean Energy Utilization Luo, Kun; Zhejiang University, Department of Energy Engineering Luo, Kai Hong; University College London, Department of Mechanical Engineering Hasse, Christian; Darmstadt University of Technology

Analysis of gas-assisted pulverised coal combustion in Cambridge Coal Burner CCB1 using FPV-LES

Yiran Chen,[†,‡] Oliver T. Stein,[*,‡] Andreas Kronenburg,[‡] Jiangkuan Xing,[¶] Kun Luo,[¶] Kai Hong Luo,[*,§] and Christian Hasse[‖]

[†]*Center for Combustion Energy, Key Laboratory for Thermal Science and Power Engineering of Ministry of Education, Department of Thermal Engineering, Tsinghua University, Beijing 100084, China*

[‡]*Institut für Technische Verbrennung, Universität Stuttgart, Herdweg 51, 70174 Stuttgart, Germany*

[¶]*State Key Laboratory of Clean Energy Utilization, Zhejiang University, Hangzhou, 310027, China*

[§]*Department of Mechanical Engineering, University College London, Torrington Place, London WC1E 7JE, UK*

[‖]*Simulation of Reactive Thermo-Fluid Systems, TU Darmstadt, Otto-Berndt-Strasse 2, 64827 Darmstadt, Germany*

E-mail: o.stein@itv.uni-stuttgart.de; k.luo@ucl.ac.uk

Abstract

Gas-assisted pulverized coal combustion in the laboratory scale Cambridge Coal Burner configuration CCB1 is studied using large eddy simulation (LES) coupled with a multi-stream flamelet/progress variable (FPV) model in an Euler-Lagrange framework.

The FPV-LES implementation is coupled with an enthalpy correction method for two-phase energy transfer. Both non-reacting and reacting (pure pilot and coal flame) cases are simulated, and the simulation results are compared with the experimental evidence. The agreement of the simulation results with the measurements is found to be reasonable, although it needs to be noted that the experimental data mainly focuses on the far upstream region where coal combustion effects are limited. The flame structures of the pure pilot flame and coal flame are carefully analysed across the entire simulation domain. Different gas flame modes are identified for the coal flame as a function of the downstream coordinate, namely typical premixed flame (far upstream), double flame (middle), and typical non-premixed flame (far downstream). The time histories of coal particles are traced to demonstrate the relation between gas flame modes and the devolatilisation process. Moreover, the average distance between the particles is used to distinguish between the group combustion mode found near the centre of the burner and the individual particle combustion mode located in the outer region of the flame, which is in agreement with the experimental observation. This study provides new insights into the flame characteristics of swirling gas-assisted pulverized coal flames and adds to the knowledge database on FPV-LES modeling of PCC.

Introduction

Power security and sustainability requirements dictate that coal will remain a major power source for many decades to come, and improved understanding of coal combustion characteristics is critical to developing cleaner combustion technologies before renewables become a major power source. Pulverized coal combustion (PCC) typically consists of several steps: particles heat up in the hot combustion environment, volatile matter releases through devolatilisation, char off-gas is generated by reactions of oxidizer with the char surface, and both gasified volatile matter and char off-gas are further oxidized homogeneously in the bulk

gas phase. The physics of the turbulent PCC process can be explored by means of numerical simulation methods including direct numerical simulation (DNS), large eddy simulation (LES) and Reynolds-Averaged Navier-Stokes (RANS) approaches. While providing the most detailed information, DNS studies that resolve all relevant scales are limited by computational capacity and therefore mainly focus on single particles[1–4] or small groups of particles in fixed arrays.[5–7] Larger scales of turbulence and relative motion both among particles and between particles and surrounding gas can only be considered by ignoring the particle boundary layers in so-called carrier-phase DNS,[8–13] but since the computational cost still remains high, this method cannot be used to study entire PCC combustors. Instead, RANS and LES methods are more suited for simulating PCC in real furnaces. Kurose et al. [14] and Edge et al. [15] compared LES and RANS results of pulverized coal combustion and demonstrated the advantages of LES over RANS. Stein et al. [16] applied both Euler-Lagrange and Euler-Euler frameworks in PCC-LES and results for a laboratory-scale coal burner showed considerable differences between the two numerical methods, but also among different Euler-Lagrange models. Generally, the Euler-Lagrange framework for PCC-LES[17–19] offers a greater flexibility for the description of particle-related effects and therefore the approach is also employed in the present work.

Directly integrating stiff ordinary differential equations (ODE) that describe complex combustion chemistry (especially with the large hydrocarbons present in coal combustion) is usually significantly more time-intensive than solving the Navier-Stokes equations alone. Hence, one of the major difficulties that RANS and particularly LES of PCC face is the computational cost for solving chemistry. Therefore, global reactions or simplified fuel compositions have been used in early simulations and turbulence-chemistry interactions have typically been closed by eddy break-up approaches, see e.g.[16,18] However, these simplifications hamper the capabilities for predicting important flame properties like ignition delay, flame temperature, flame propagation speed and pollutant formation.

A more advanced method for modeling turbulence-chemistry interactions is the flamelet

approach that has widely been applied in single phase gas combustion. Recent studies show that the flamelet progress variable (FPV) model[20] can be extended for coal combustion. Watanabe et al. [21] treated coal combustion as a double-stream FPV problem which includes a volatile stream and a char off-gas stream to describe the heterogeneous processes. Vascellari et al. [22] applied the FPV method to recover the dynamic ignition process of a single coal particle from DNS. Messig et al. [23] and Wen et al. [24] simulated coal combustion in a laminar counterflow to compare the FPV method with reference results from full transport and direct chemistry integration, and found a good agreement. Yamamoto et al. [25] simulated a coal jet flame in a lab-scale burner using FPV and an eddy dissipation concept model and found the FPV results to be closer to experimental data. Similarly, Rieth et al. [26,27] and Knappstein et al. [28,29] have demonstrated the high accuracy and computational affordability of flamelet methods for PCC-LES. Following up on this recent success of the FPV modelling framework, the FPV-LES method is employed to investigate PCC in the present study.

In addition to these advances in numerical modelling, recent progress on measurement techniques for state-of-the-art experimental investigations of coal combustion has led to a detailed experimental knowledge database, see for example.[30–34] In particular, a considerable number of experimental studies of PCC supported by gaseous pilot flames, i.e. *gas-assisted coal combustion* has recently been reported. This is because gas-assisted coal flames offer a suitable compromise between ensuring a clean environment for reliable laser-based diagnostics, while still capturing the major physics occurring in PCC.[35–37] In light of this, the Cambridge Coal Burner (CCB) configuration offers reliable experimental data on a novel gas-assisted swirling coal flame. The burner has been characterised in detail experimentally by means of Laser doppler velocimetry (LDV) and high-speed stereo particle image velocimetry (PIV).[38,39] Results from a first numerical simulation have been published,[40] albeit only for the non-reacting experimental conditions. The objectives of the present work are therefore threefold and can be summarised as follows

- Apply the FPV-LES framework to the well-characterised Cambridge coal flame CCB1

- Enhance the knowledge database on gas-assisted coal combustion by analysing pilot and coal flame contributions
- Perform detailed analyses of the flame structure and particle dynamics which are not yet well understood

To this end, we apply the FPV-LES model to the three experimental cases available for CCB1, namely non-reacting, pure pilot and coal combustion conditions, perform a careful validation against experiments and present detailed analyses of the numerical results.

Modelling

FPV-LES governing equations

The FPV model is based on the assumption that the thermo-chemical state of the reacting flow can be determined by using a limited number of control variables.[20] Hence, the filtered transport equations for continuity, momentum and FPV control variables are solved in the LES framework. The control variables are mixture fractions Z_k, reaction progress variable Y_C and total enthalpy h. In the present context of two-phase reacting flow an Euler-Lagrange method is implemented by introducing a set of Lagrangian equations for particle evolution and considering Lagrangian source terms $\dot{S}_\gamma$ for mass, momentum and heat transfer in the Eulerian transport equations, where γ denotes the specific equation. After closure, the LES-filtered governing equations of the gas phase read

$$\frac{\partial \overline{\rho}}{\partial t} + \frac{\partial}{\partial x_i}\left(\overline{\rho}\widetilde{u}_i\right) = \dot{S}_\rho \tag{1}$$

$$\frac{\partial \overline{\rho}\widetilde{u}_i}{\partial t} + \frac{\partial}{\partial x_j}\left(\overline{\rho}\widetilde{u}_i\widetilde{u}_j\right) = \frac{\partial}{\partial x_i}\left(\left(\mu + \mu_{\mathtt{sgs}}\right)\left(\frac{\partial \widetilde{u}_j}{\partial x_i} + \frac{\partial \widetilde{u}_i}{\partial x_j} - \frac{2}{3}\frac{\partial \widetilde{u}_k}{\partial x_k}\delta_{ij}\right)\right) + \frac{\partial p}{\partial x_i} + \dot{S}_{u_i} \tag{2}$$

$$\frac{\partial \overline{\rho}\widetilde{Z}_k}{\partial t} + \frac{\partial}{\partial x_i}\left(\overline{\rho}\widetilde{u}_i\widetilde{Z}_k\right) = \frac{\partial}{\partial x_i}\left(\left(\frac{\mu}{\mathtt{Sc}} + \frac{\mu_{\mathtt{sgs}}}{\mathtt{Sc}_t}\right)\frac{\partial \widetilde{Z}_k}{\partial x_i}\right) + \dot{S}_{Z_k} \tag{3}$$

$$\frac{\partial \overline{\rho}\widetilde{Y}_C}{\partial t} + \frac{\partial}{\partial x_i}\left(\overline{\rho}\widetilde{u}_i\widetilde{Y}_C\right) = \frac{\partial}{\partial x_i}\left(\left(\frac{\mu}{\mathtt{Sc}} + \frac{\mu_{\mathtt{sgs}}}{\mathtt{Sc}_t}\right)\frac{\partial \widetilde{Y}_C}{\partial x_i}\right) + \widetilde{\dot{\omega}}_{Y_C} + \dot{S}_{Y_C} \tag{4}$$

$$\frac{\partial \overline{\rho}\widetilde{h}}{\partial t} + \frac{\partial}{\partial x_i}\left(\overline{\rho}\widetilde{u}_i\widetilde{h}\right) = \frac{\partial}{\partial x_i}\left(\left(\alpha + \alpha_{\mathtt{sgs}}\right)\frac{\partial \widetilde{h}}{\partial x_i}\right) + \dot{S}_h + \dot{S}_{rad,g}, \tag{5}$$

where standard nomenclature for combustion LES has been employed and $\dot{S}_{rad,g}$ is the radiative source term of the gas phase. The Smagorinsky model[41] is employed for subgrid closure. The total enthalpy of the mixture is defined as the sum of chemical and sensible enthalpy ($h = \sum_{j=1}^{n} h_{c_j} Y_j + \int_{T_0}^{T} C_{p,mix} dT$). In systems with multiple fuel streams, more than a single mixture fraction is needed. Hence, Eq. (3) describes the evolution of general mixture fraction variables Z_k which may have various physical meanings depending on the specific case set-up. As a result, the physical definition of Z_k and its Lagrangian source term $\dot{S}_{Z_k}$ depends on the fuel stream associated with it. For example when Z_k refers to the coal volatile stream $\dot{S}_{Z_k}$ represents the fuel stream containing the volatiles. In cases without mass release from the Lagrangian particles (e.g. pure pilot flame) $\dot{S}_{Z_k} = 0$. It is noted that due to the lack of recirculation in the studied coal flame CCB1 the residence time of the coal particles in the hot region is comparatively low and virtually no char conversion occurs.[38,39] As a result, the modelling framework presented below does not consider any char conversion sub-models. The reaction progress variable Y_C is defined as a linear combination of species mass fractions, with $Y_C = Y_{\mathrm{CO}} + Y_{\mathrm{CO_2}} + 0.5 Y_{\mathrm{H_2O}}$. The term $\widetilde{\dot{\omega}}_{Y_C}$ in Eq. (4) represents the source term of the reaction progress variable and is retrieved from the flamelet library. The interphase source terms for momentum and enthalpy are

$$\dot{S}_{u_i} = \frac{1}{V}\sum_{j}^{n_p} N_j \left[\frac{d\left(m_p u_{i,p}\right)}{dt}\right]_j \tag{6}$$

$$\dot{S}_h = \frac{1}{V}\sum_{j}^{n_p} N_j \left[\mathrm{Nu}\kappa\pi d_p \left(T_c - T_p\right) + \frac{dm_p}{dt} h_{vol}\left(T_p\right)\right]_j, \tag{7}$$

where n_p is the number of parcels[40] in an Eulerian LES cell, the index j refers to the jth parcel and N_j to the number of particles in parcel j. The latter is calculated based on the mass flux of coal through the burner and varies for particle groups of different size, with on average 8.6 coal particles per parcel. The subscript p denotes a Lagrangian particle (parcel) quantity, the subscript c implies a continuous phase (gas) quantity and vol refers to the volatile species. V is the Eulerian cell volume, κ is a (film) thermal conductivity and the Nusselt number Nu is defined in terms of particle Reynolds number Re_p and Prandtl number Pr as

$$\mathrm{Nu} = 2.0 + 0.6\mathrm{Re}_p^{1/2}\mathrm{Pr}^{1/3}. \tag{8}$$

The source term of the continuity equation equals the source term associated with mass release from devolatilisation

$$\dot{S}_\rho = \dot{S}_{vol} = \frac{1}{V}\sum_j^{n_p} N_j \left[\frac{dm_{p,vol}}{dt}\right]_j. \tag{9}$$

The interphase source term of the volatile species is computed as

$$\dot{S}_{Y_k} = \dot{S}_{vol} Y_{k,vol}, \tag{10}$$

where $Y_{k,vol}$ refers to the mass fraction of the kth species in the volatile matter. Considering Eq. (10) and based on our definition of the reaction progress variable its source term is computed as

$$\dot{S}_{Y_C} = \dot{S}_{Y_{\mathrm{CO}}} + \dot{S}_{Y_{\mathrm{CO_2}}} + 0.5\dot{S}_{Y_{\mathrm{H_2O}}}. \tag{11}$$

It is assumed that particle mass changes solely due to devolatilisation, particle momentum because of drag, and particle temperature due to convective heat transfer and heat exchange associated with pyrolysis. Hence, the governing equations of the Lagrangian coal particles (parcels) read

$$\frac{dm_p}{dt} = \frac{dm_{vol}}{dt} \tag{12}$$

$$\frac{d\mathbf{U}_p}{dt} = -\frac{3\rho_c C_D}{4\rho_p d_p} |\mathbf{U}_p - \mathbf{U}_c| (\mathbf{U}_p - \mathbf{U}_c) \tag{13}$$

$$\frac{dT_p}{dt} = \frac{6\mathrm{Nu}\kappa (T_c - T_p)}{\rho_p d_p^2 c_{p,p}} - \frac{dm_{p,vol}}{dt}\frac{\Delta h_{pyr}}{m_p c_{p,p}} + \dot{S}_{rad,p}, \tag{14}$$

with the particle diameter d_p, heat of pyrolysis Δh_{pyr}, radiative source term of the particles $\dot{S}_{rad,p}$ and otherwise standard nomenclature. The drag coefficient C_D is calculated as[42]

$$C_D = \min\left[\frac{24}{\mathrm{Re}_p}\left(1 + \frac{1}{6}\mathrm{Re}_p^{2/3}\right), 0.424\right]. \tag{15}$$

Coal submodels and chemistry

The thermophysical properties and coal composition used in this study follow the data from the relevant experiment.[38] An assumption is made that the major tar species is C_6H_6.[7,43,44] A typical set of small hydrocarbons is assumed for the light volatile species and the mass fractions of species in the volatile matter are computed based on conserving the LHV of the coal and elemental mass. The major coal particle properties are given in Tab. 1. The

Table 1: Coal particle properties.

Density	640 kg/m^3
Injection rate	0.6 g/s
Composition, mass fractions (after Q-factor adjustment)	
Volatiles	0.5516
Char	0.3835
Ash	0.0649
Volatile Species, mass fractions	
C_6H_6	0.438737
CO	0.312110
CH_4	0.142145
C_2H_2	0.063135
H_2	0.018548
N_2	0.025325
Heat of pyrolysis	1.9897e6 J/kg

CRECK52 mechanism[43,45] which contains 52 species and 452 reactions is used for homogeneous chemistry. The coal particle density is assumed to remain constant during combustion,

so the mass release due to pyrolysis will result in (mild) particle shrinking. Further effects that could lead to coal swelling or shrinking (e.g. breakage) are ignored based on similar reasoning as in[46] where a comparable case was studied. A single kinetic rate is applied to describe devolatilisation

$$\frac{dm_{vol}}{dt} = A \exp\left(\frac{-E_a}{RT_p}\right) m_{p,vol}, \tag{16}$$

where $m_{p,vol}$ is the volatile mass remaining in the coal particle. The pre-exponential factor and activation energy $A = 4.414 \times 10^{11} s^{-1}$ and $E_a = 1.657 \times 10^8 J/kg$ have been obtained by fitting the single rate expression to results from CPD[47] for a typical heating rate in the burner. Thus, Q-factor adjustment was conducted based on the detailed CPD predictions.

The particle size is assumed to follow a Rosin-Rammler distribution with a mean diameter $\overline{d}_p = 50$ μm and spread parameter $n = 2.0$ for freshly-injected particles. However, Euler-Lagrange methods require the particle diameter to be much smaller than the Eulerian cell size. Conversely, transporting very small particles may negatively affect simulation stability. Hence, the set of initialised particle sizes is restricted to the range 20...80μm. To test the effect that the commonly used assumption of injecting a uniform particle size would have, an additional simulation is performed assuming a single $d_p = 50\,\mu$m for all injected particles, cf. results section.

The P1 radiation model[48] is introduced to consider thermal radiation. In the P1 approach the integro-differential radiative transfer equation (RTE) for the radiation intensity I is replaced by a differential transport equation for the incident radiation G that is affected by absorption, emission and scattering of both the gas phase and the coal particles. A grey mean coefficient model based on temperature polynomials of absorbing gas species is chosen for mixture absorptivity.[49] Once the incident radiation G has been computed, it is used to calculate the radiative source terms of the gas and particle phase, i.e. $\dot{S}_{rad,g}$ in Eq. (5) and $\dot{S}_{rad,p}$ in Eq. (14).

Flamelet modelling

Flamelet tables are generated by computing a series of one-dimensional counterflow flames using the in-house code pyFLUT developed at TU Darmstadt. Two flamelet libraries are created, one for the pure pilot flame (library 1) and one for the coal flame (library 2), see Tab. 2.

Table 2: Definition of progress variable and mixture fractions

Definition	library 1	library 2
Y_C	$CO+CO_2+0.5H_2O$	
Z_1	CH_4/air mixture	
Z_2	None	volatile stream

Library 1 (pure pilot flame)

For the pure pilot flame only one type of fuel (CH_4) needs to be considered and all heterogeneous effects are absent, such that a single conserved scalar mixture fraction $Z = Z_1$ can be used, the fuel and oxidizer composition of which are fixed. In laminar counterflow combustion reaction progress is a function of the mass flow from the opposed nozzles (at fixed nozzle separation) and may be expressed by (either of) mass flow rate $\dot{m}$, scalar dissipation χ, or reaction progress variable Y_C. Here, counterflow flames in physical space are generated as a function of $\dot{m}$ first and subsequently mapped to progress variable space, such that the reacting scalar fields become functions of mixture fraction and progress variable only $Y_i = Y_i(Z, Y_C)$, where $Z = Z_1$. To consider subgrid effects in LES of turbulent flow a presumed beta-PDF based on the filtered mixture fraction $\widetilde{Z}$ and the subgrid mixture fraction variance $\widetilde{Z''^2}$ is employed. Following Pierce and Moin[20] the sub-grid variance is modelled from the resolved gradient of mixture fraction

$$\widetilde{Z''^2} = C_Z \Delta^2 \left(\frac{\partial \widetilde{Z}}{\partial x_i} \right)^2 \tag{17}$$

with filter width Δ and $C_Z = 1$.[50] As customary in flamelet-LES of PCC subgrid distributions of all governing variables other than mixture fraction (here: reaction progress variable) are ignored, see e.g. Rieth et al.[26] As a result, the filtered species mass fractions of library 1 can be obtained by multiplying $Y_i(Z, Y_C)$ with the PDF of Z and integrating across mixture fraction space

$$\widetilde{Y}_i\left(\widetilde{Z}, \widetilde{Z''^2}, \widetilde{Y_C}\right) = \int_0^1 Y_i\left(Z, Y_C\right) P\left(Z\right) dZ. \tag{18}$$

Library 2 (coal flame)

Prior to the final simulations of the coal case an extented flamelet model that includes char conversion[51,52] was invoked to test the occurrence of char conversion in the CCB1 configuration. Despite the added swirl, flame CCB1 does not feature any major recirculation zones and burns similarly to a jet flame, such that particle residence times are too short for significant char conversion to occur. Our tests with the extended flamelet model therefore confirmed the experimental finding that char combustion effects are small, and can in fact be ignored for the CCB1 flame studied here. Based on this observation,

mixture fraction Z_1 in library 2 is (again) a conserved scalar associated with CH_4/air from the pilot and the central jet, whereas Z_2 describes the heterogeneous release of volatiles and their mixing with air. Following the ideas of Watanabe et al.[21] the one-dimensionality of the flamelet is retained by considering a total mixture fraction

$$Z = Z_1 + Z_2 \tag{19}$$

and the mixing ratio

$$A_Z = \frac{Z_1}{Z} = \frac{Z_1}{Z_1 + Z_2}, \tag{20}$$

where the latter is used to adjust the fuel side of the counterflow flames during flamelet tabulation according to

$$Y_{\text{fuel}} = A_Z Y_{\text{CH}_4/air} + (1 - A_Z) Y_{\text{vol}}. \tag{21}$$

After applying subgrid modelling analogously to library 1, the filtered species mass fractions from library 2 can be retrieved as

$$\widetilde{Y}_i\left(\widetilde{Z},\widetilde{Z''^2},\widetilde{Y_C},A_Z\right)=\int_0^1 Y_i\left(Z,A_Z,Y_C\right)P\left(Z\right)dZ. \tag{22}$$

The flamelet table is discretised by using 400 x 20 x 100 x 20 support points in the $\widetilde{Z}$, $\widetilde{Z''^2}$, $\widetilde{Y_C}$ and A_Z direction, respectively.

Treatment of enthalpy variations

Based on the assumption that for a low coal/air ratio (dilute two-phase flow) the heat exchange between the gas and the particles mainly affects flame temperature but has little effect on species space, Messig et al. [23] proposed a "temperature correction" method for PCC flamelet calculations. Retaining that assumption, here we adopt an "enthalpy correction" method and base it on correcting the filtered sensible enthalpy $\widetilde{h}_s$ rather than directly modifying temperature, which better suits the structure of the simulation code employed in this study (OpenFOAM).[53] The filtered mixture sensible enthalpy $\widetilde{h}_s$ is calculated from the filtered total enthalpy $\widetilde{h}$ (available from transport Eq. (5)) and the chemical enthalpies of the species $h_{c,j}$ as

$$\widetilde{h}_s=\widetilde{h}-\sum_{j=1}^{n}\widetilde{Y}_j h_{c,j}, \tag{23}$$

where the filtered species mass fractions $\widetilde{Y}_j$ are retrieved from the FPV library. Sensible enthalpy h_s is a polynomial function of T

$$h_s\left(T\right)=\int_{T0}^{T}C_{p,mix}\left(x\right)dx \tag{24}$$

$$C_{p,mix}=\sum_{i=0}^{7}c_i T^i, \tag{25}$$

and a Newton-Raphson method is applied to update mixture temperature. Finally, the gas density $\rho(T)$ is updated according to the ideal gas law. The employed method considers heat transfer both due to (convective) heat exchange between the particles and the gas phase, and due to radiation, since both effects are included in the transport equation for the total enthalpy of the gas, Eq. (5). Hence, mixture enthalpy $\widetilde{h}$ is altered and enters Eq. (23), which will lead to the correction of gas temperature and density.

Simulation set-up

Experimental background

The experiment under consideration is the Cambridge Coal Burner[38,39] which is available in two different configurations. Here, the configuration CCB1 is solely considered and a schematic diagram is shown in Fig. 1. The burner consists of a central nozzle where coal can

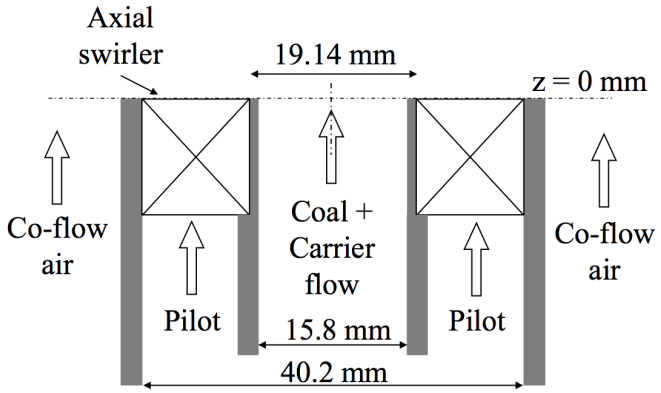

Figure 1: Schematic diagram of the CCB1 experiment[38]

be injected within a carrier gas stream which is surrounded by an annular pilot channel with swirl (swirl number 0.77) and an outer co-flow stream of air. In the CCB1 experimental campaign[38] three considerably different cases were studied, namely (i) non-reacting gas, (ii) pure pilot combustion of CH_4 and (iii) gas-assisted coal flame. For all cases, co-flow air is injected at 4.736 g/s. In the non-reacting case, there is no CH_4 in any stream. In the two

reacting cases -both gas and coal- CH_4 is added to the air flow through the central nozzle at a mass flow rate of 0.033 g/s, which corresponds to a lean mixture with equivalence ratio $\phi = 0.322$. For both reacting cases the pilot stream issues a stoichiometric CH_4/air mixture. The sole difference between the pure pilot case and the coal flame is that in the latter configuration, coal particles are injected jointly with the gas through the central nozzle, at a mass flow rate of 0.6 g/s. For convenience the mass flow rates of gas through the burner nozzles for all cases are summarised in Tab. 3. The experimental velocity field was measured by both LDV and PIV.[38] While the two measurement techniques showed slight differences due to the slip of larger coal particles in PIV, the results from both methods were overall similar and the LDV data is used to compare with the results from the present simulations. The nominal error in the experimental LDV measurement data is 1.4 % and 1.8 % for the mean and rms velocity, for a 95 % confidence interval .[38]

Table 3: Mass flow rates [g/s] of gas through the burner nozzles for the three considered cases.[38] For the coal flame an additional 0.6 g/s of coal are injected via the central nozzle.

case	central air	central CH_4	pilot air	pilot CH_4	co-flow
non-reacting gas	1.776	0	1.308	0	4.736
pure pilot flame	1.750	0.033	1.184	0.069	4.736
coal flame	1.750	0.033	1.184	0.069	4.736

Computational domain and boundary conditions

The computational domain is a cylinder with a diameter of 320 mm and a length of 550 mm, see Fig. 2. The complex geometry of the swirler upstream of the pilot exit is considered in detail, by generating the simulation mesh from the available geometric CAD data for the swirler. The mesh consists of 5 million non-uniform with cell sizes ranging from 0.1 mm near the nozzle exit to 4 mm near the outlet boundary. The maximum ratio of sub-grid kinetic energy to resolved kinetic energy is 0.08, thus the mesh is assumed to be fine enough for LES. At the lateral boundary a no-slip wall boundary condition is employed. Although the experimental configuration is unconfined, with a diameter ratio 160:7.9 these side walls are far

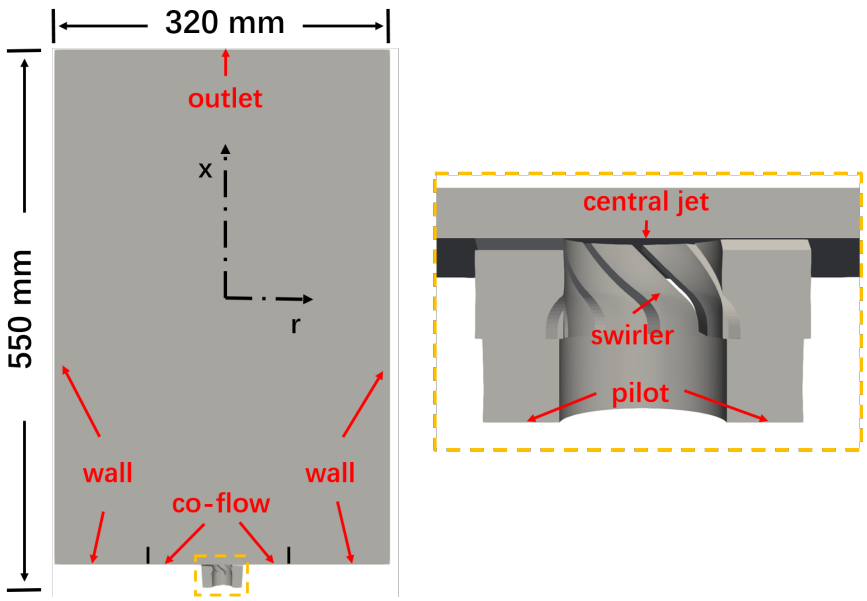

Figure 2: Clipped view of the computational domain and boundary patches

away from the central jet and do not affect the flame. To provide transient inflow boundary conditions for LES a-priori simulations of fully-developed turbulent pipe flow are conducted and superimposed on the central nozzle at every time step of the flame simulation. For the coal flame fuel particles are added to the central nozzle and initialised with the velocity of the injected carrier gas. Since the swirling flow through the pilot is included in the flame

Table 4: Inlet boundary conditions for the governing flamelet variables. When using library 1 (pure pilot) Z_2 is not transported. When library 2 (coal flame) is used Z_2 denotes volatiles, but set to zero at the boundaries.

Boundary	Z_1 (gas fuel/air mixture)	Z_2 (volatiles)	h (J/kg)	Y_C
central	0.085335	0/none	-85748.8	0
pilot	0.25	0/none	-254458	0
co-flow	0	0/none	1907.6	0

simulation, a constant velocity profile corresponding to the experimental mass flow rate of gas is employed at the pilot inlet patch. The mass flow rates of gas through the nozzles differ for different cases, cf. Tab. 3. The boundary conditions for the governing variables of the FPV model are provided in Tab. 4. Here $Z_1 = 1$ refers to a mixture with mass fractions CH_4: 0.220978, O_2: 0.181448, N_2: 0.597575 and $Z_{st} = 0.25$. These values are chosen to avoid

the tabulation of unnecessary states in the chemistry library: since Z_1 is a conserved scalar it has no interphase source term and values $Z_1 > Z_{1,st}$ do not occur in the simulation.

Initialisation of the flame

It is emphasised here that -in line with the experiments- the pilot boundary condition is cold, stoichiometric CH_4/air reactants. Alternatively, a mixture of hot combustion products from CH_4/air combustion could be assumed to issue from the pilot nozzle exit. Such an alternative boundary treatment has also been tested in the simulation campaign. However, due to the inherent geometrical coupling of axial and circumferential momentum with the given experimental swirler geometry, such a hot inlet stream with low density and high velocity results not only in higher axial, but also increased circumferential velocities above the pilot nozzle exit. A preliminary test of this alternative boundary condition led to significant over-predictions of the mean circumferential velocity above the pilot (not shown for brevity) and such boundary treatment is thus avoided here. Instead, a stoichiometric CH_4/air reactant mixture is injected through the pilot boundary and consequently a numerical procedure for flame ignition is required.

Ignition is modelled by adding an artificial source term to the progress variable equation at the beginning of the reacting simulations. The employed ignition kernel is a spherical region of diameter $d_{ign} = 0.19d$ located just above the pilot nozzle exit at axial location x/d=0.63, radial location r/d=0.63 and an arbitrarily chosen circumferential angle due to axisymmetry. The source term is defined as

$$\dot{S}_{Y_{C,ign}} = A_{ign} \left(Y_{C,max} - Y_C \right) \tag{26}$$

in the ignition region, with a rate constant $A_{ign} = 500$ and maximum progress variable $Y_{C,max}$. The source term is active during the first 5 ms of the simulation and switched off

thereafter. Due to this enforced increase of Y_C, the temperature inside the ignition kernel will rise, as read from the flamelet library. The flame can then propagate away from the ignition location and finally reach a steady burning state, where it is anchored above the pilot exit, see Fig. 7. It has been verified that slight variations of the employed ignition kernel parameters (i.e. location and rate constant A_{ign}) will not unduly affect the steady-state anchoring position of the flame. Since statistical sampling is solely conducted at steady state, any possible errors associated with this simplified ignition procedure will not affect the final statistical results or conclusions.

Solver details

The solver is developed based on the open-source C++ platform OpenFOAM version 2.4.x. A second-order backward scheme is used for time marching and a limitedLinear (TVD) scheme is chosen for convection. A second-order linear interpolation scheme is used for the diffusion terms. The simulations of the coal flame typically use 30 Intel E5-2697 12-core processors with a total of 360 cores and 24,000 CPUh.

Results and Discussion

Experimental validation

In the experimental campaign for CCB1 radial profiles of the mean and RMS velocity components in the axial, radial and circumferential coordinate direction were measured at four axial locations by means of LDV.[38] The corresponding LES gas velocity fields are transformed from Cartesian to cylindrical coordinates for comparison with experiments as shown in Figs 3 - 5. All references to spatial distance have been normalised by the inner diameter of the central jet ($d = 15.8\,\text{mm}$), such that the measured axial locations 2, 10, 30 and 50 mm correspond to $x/d = 0.13$, 0.63, 1.90 and 3.16, respectively.

For the non-reacting case shown in Fig. 3, it can be observed that far upstream at $x/d =$

0.13 the predicted mean velocity components are lower than the experimental results in the region $0.6 \leq r/d \leq 1.2$, i.e. above the exit of the pilot stream. However, at all downstream

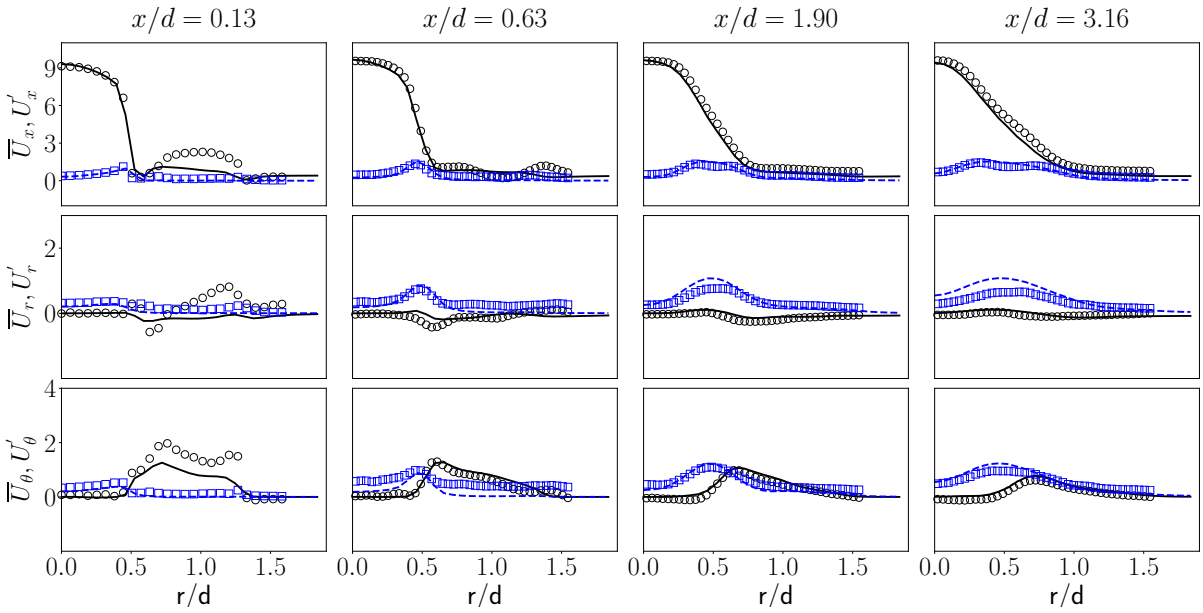

Figure 3: Non-reacting case: Radial profiles of mean (black) and RMS (blue) velocity [m/s]. The axial, radial and circumferential velocity are denoted as U_x, U_r and U_θ.

locations, the LES velocity profiles match the measurements very well. Overall, the quality of the non-reacting LES predictions is comparable to the only previous numerical study of this burner reported by Muto et al. [40] The LES predictions for the pure pilot case are shown in Fig. 4. It can be observed that the upstream LES results directly above the burner at $x/d = 0.13$ are better than for the non-reacting case, whereas the downstream predictions are reasonable, but show somewhat stronger deviations from the experimental data than the non-reacting case. The predictions of the pure pilot flame indicate a stronger mean dissipation in the axial, but weaker dissipation in the circumferential direction. The same applies to the coal flame results that are presented in Fig. 5, i.e. the upstream predictions at $x/d = 0.13$ are good, whereas the downstream predictions show a stronger decay of the mean axial velocity (particularly at high radii) and the mean swirling velocity is over-predicted. Overall the velocity predictions of this complex turbulent reacting flow (both pure pilot, Fig. 4, and coal flame, Fig. 5) are found to be in reasonable agreement with the experimental

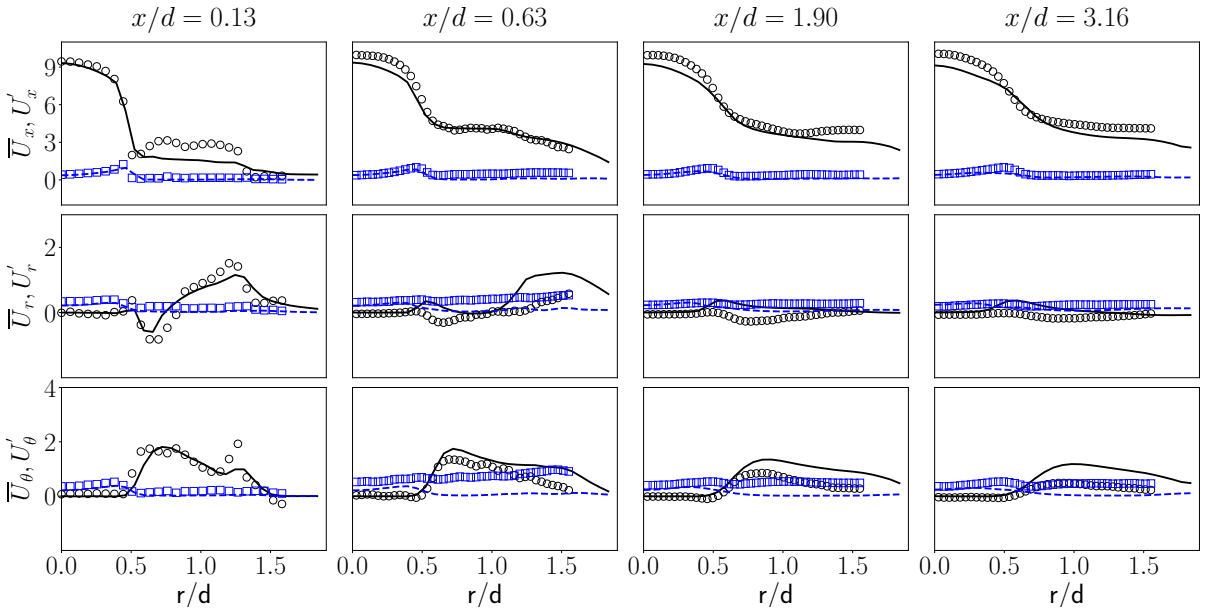

Figure 4: Pure pilot case (library 1): Radial profiles of mean (black) and RMS (blue) velocity [m/s]. The axial, radial and circumferential velocity are denoted as U_x, U_r and U_θ.

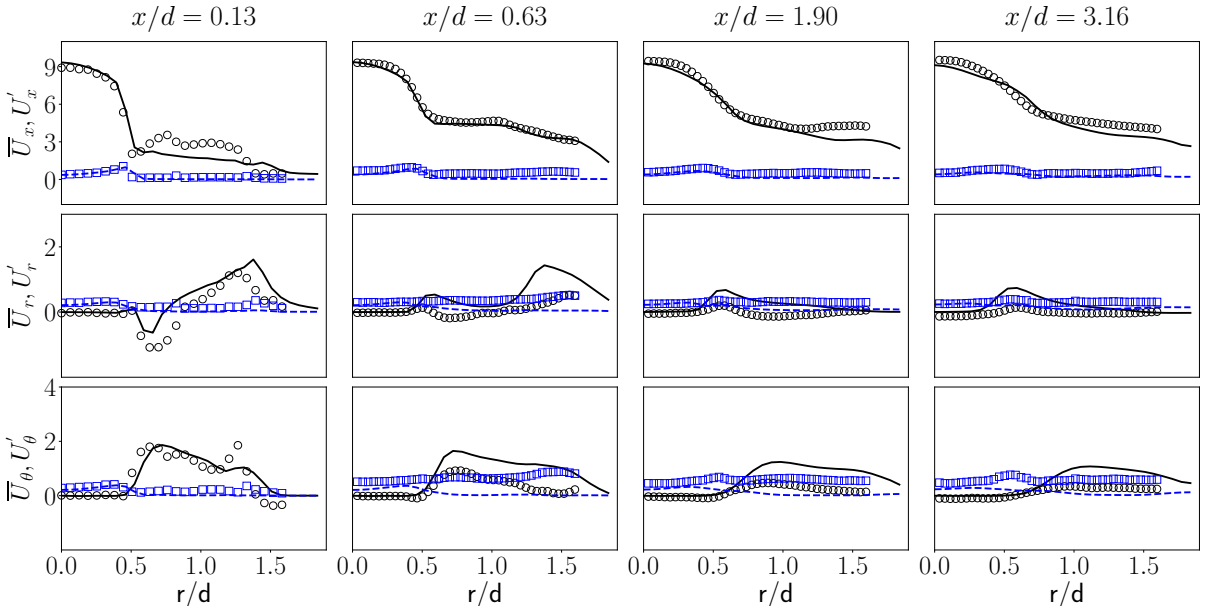

Figure 5: Coal flame (library 2): Radial profiles of mean (black) and RMS (blue) velocity [m/s]. The axial, radial and circumferential velocity are denoted as U_x, U_r and U_θ.

evidence.

The fact that the prediction quality for the pure pilot and the coal flame case is very similar is not surprising. This is because the experimental campaign mainly considered the near-burner region with the most downstream measurement position located at about three

nozzle diameters from the burner exit plane. Since after injection the coal particles require some time to heat up and ignite, only a limited number of them is already burning within the measurement region such that the pilot and the coal flame in this area are similar. This is confirmed by calculating the average extent of devolatilisation of all coal particles in thin (2 mm) horizontal slices at downstream positions $0 \leq x/d \leq 3.16$, i.e. along the entire measurement region. The maximum average devolatilisation extent (not shown) is located at $x/d = 3.16$ and amounts to 17.5%. This finding is corroborated by our subsequent analysis of the flame structure, which therefore mainly focuses on the area further downstream, where the differences between the pure pilot and the coal flame become more apparent.

Flame structure analysis

A first qualitative impression of the coal flame structure can be obtained by comparing experimental images to a reconstruction of the flame predicted by FPV-LES as shown in Fig. 6. It can be observed that the complex shape of the experimental pilot flame is represented

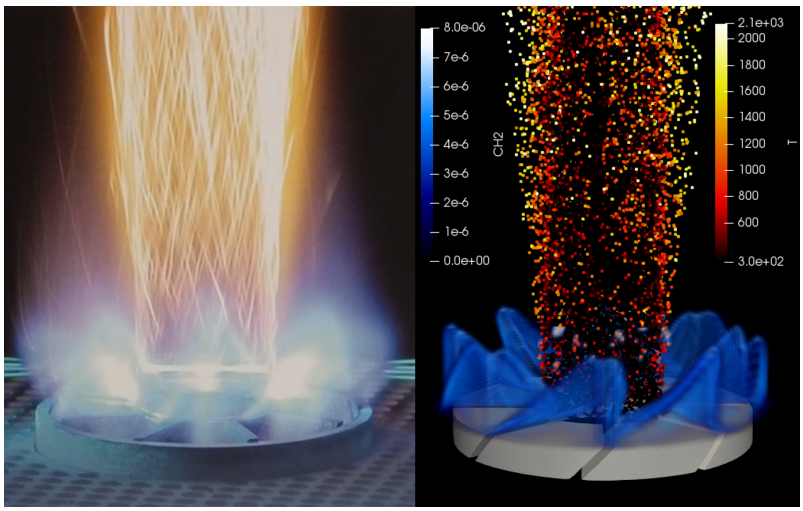

Figure 6: Experimental snapshot of coal flame CCB1 (left) and reconstructed LES snapshot (right), where the predicted flame is visualised using coal particles coloured by their temperature and the pilot flame is volume-rendered based on the CH_2 radical.

well in the simulation, as the latter includes the details of the swirler geometry in the pilot stream. The experimental image shows that the majority of observable coal particles burns

near the edge of the inner jet and the yellow streaks suggest that mainly individual particle combustion occurs in this region. This question on the prevalent regime of coal particle combustion will be revisited in more detail later.

Figure 7 compares the flame structure of the pure pilot case to the one of the coal flame. On the left of Fig. 7 the predicted gas temperatures of the two cases are compared. As

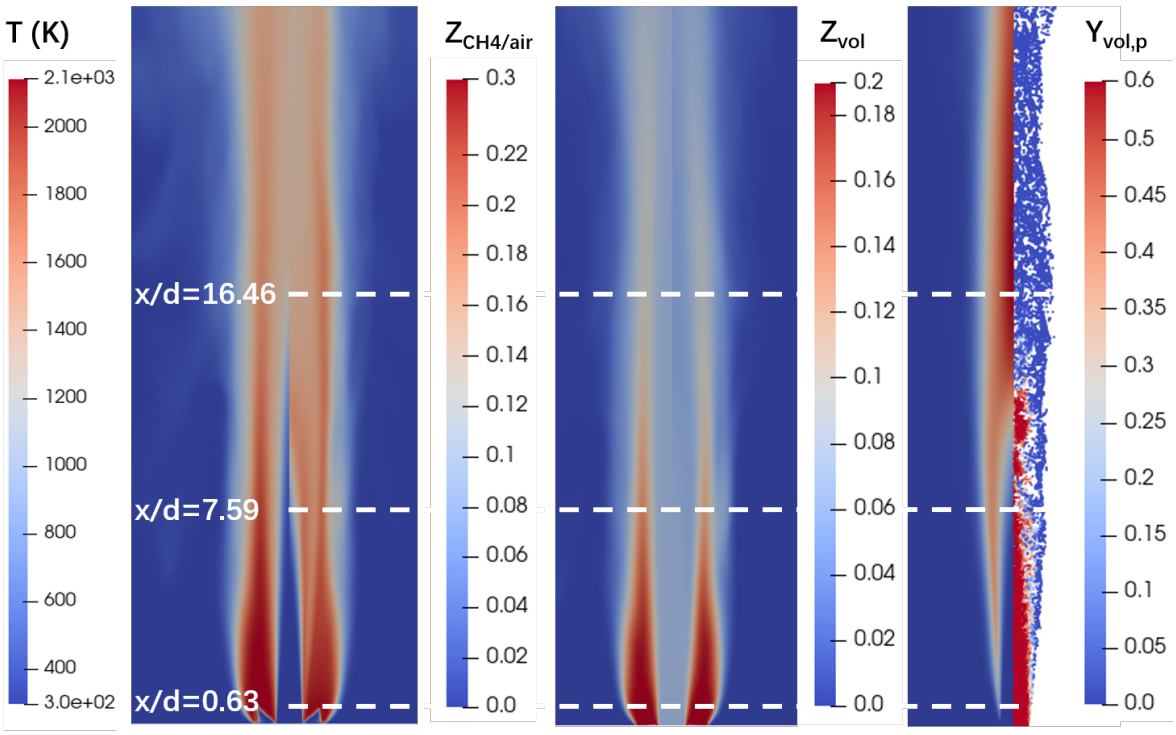

Figure 7: Comparison of the pure pilot and coal flame. Left: comparison of gas temperature, middle: comparison of pilot/CH_4 mixture fraction $Z_{\mathrm{CH}_4/air}$, right: volatile mixture fraction Z_{vol} and instantaneous mass fraction of volatiles inside the coal particles $Y_{vol,p}$ for the coal flame.

already stated in the previous section the upstream (measurement) region of both flames is dominated by the pilot such that the temperature contours are similar. However, further downstream the pure pilot and coal flame differ in terms of flame structure as discussed below. The comparison of $Z_{CH4/air}$ contours in Fig. 7 (middle) reveals fairly similar distributions of the pilot stream mixture fraction, which is expected since identical mass flow rates for the pilot stream reactants have been used for both cases, cf. Tab. 3. Note again that although $Z_{CH4/air}$ is non-zero in the central jet as the latter contains methane, this mixture is too

lean to burn without adding more fuel. Figure 7 (right) shows the volatile mixture fraction Z_{vol} and the instantaneous mass fraction of volatiles in the particles $Y_{vol,p}$ for the coal flame only. It can be observed that devolatilisation starts upstream from around $x/d = 0.63$ for the outer particles. In the middle region around $x/d = 7.59$ the released volatile matter mixes with the initially lean gas mixture in the central jet, such that homogeneous reactions can proceed and the inner side gas temperature in the coal case increases faster than in the pure pilot case. Further downstream at $x/d = 16.46$ all volatile matter has been completely released and mixing of the volatile fuel with the available oxidizer proceeds, followed by combustion.

Figure 8 compares contours of OH mass fraction between the pure pilot and coal combustion cases. In the far upstream region very little volatile release occurs such that the radical pool is controlled by the premixed flame from the pilot and the difference between the two cases is small. As already discussed for Fig. 7 this is followed by devolatilisation, fuel-oxidizer mixing and volatile combustion for the coal case, which leads to additional OH production near the central jet. As a result a double-flame structure with two distinct OH peaks along the radius can be observed at intermediate downstream positions. Far downstream, where most of the volatile matter has been released there is insufficient air in the central jet for the volatiles to burn and the inner flame region (OH peak) ceases to exist. However, the volatiles continue to mix with the available oxygen from the co-flow and an outer diffusion flame structure is formed.

To better illustrate the variation of the local flame structure with downstream distance for the pure pilot and the coal case Fig. 9 shows time-averaged line plots of gas temperature and major species mass fractions along the flame normal direction as defined by the temperature gradient. In line with Fig. 8 three combustion modes can be found in the coal flame case: (1) Typical premixed flame mode (Fig. 9(a), 9(d)), in which heat release is dominated by the combustion of the stoichiometric CH_4/air mixture from the pilot stream and coal combustion has no effect due to a lack of coal particles in this region. As a result, the line

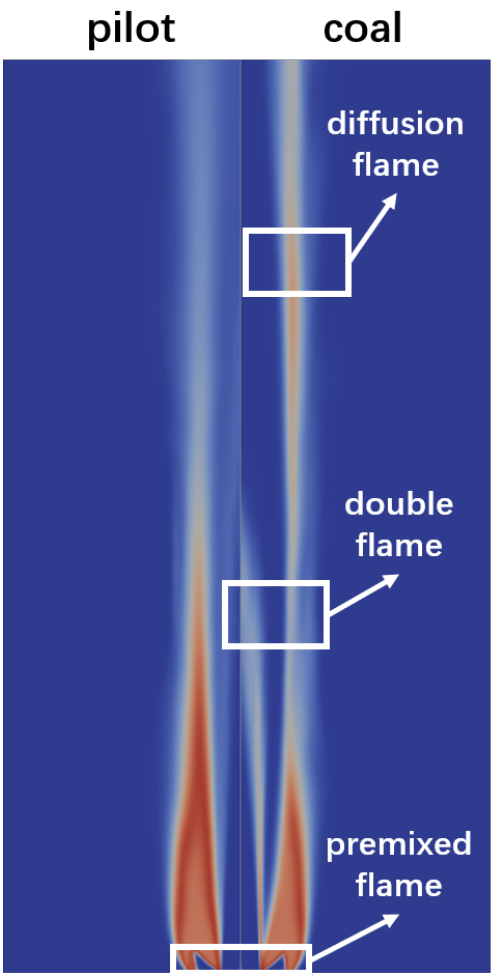

Figure 8: Comparison of the pure pilot (left) and coal flame (right), contour plot of the OH radical mass fraction.

plots from the pure pilot and coal flame are identical. (2) Double-flame mode (Fig. 9(e)), where volatiles species (mainly CO, as C_6H_6 is decomposed soon after devolatilisation) mix with the available oxidizer on both sides of the area where they are released, triggering reaction in the initially fuel-lean central jet on the inner side and on the outer side, where they form a secondary non-premixed flame due to mixing with the co-flow. Obviously, this double flame structure is only present for the coal flame (Fig. 9(e)), but absent in the pure pilot case (Fig. 9(b)). (3) Typical diffusion flame mode (Fig. 9(f)). Far downstream the central air has been completely consumed for the coal case, and the unburnt volatile fuel mixes with the co-flowing air forming a typical diffusion flame.

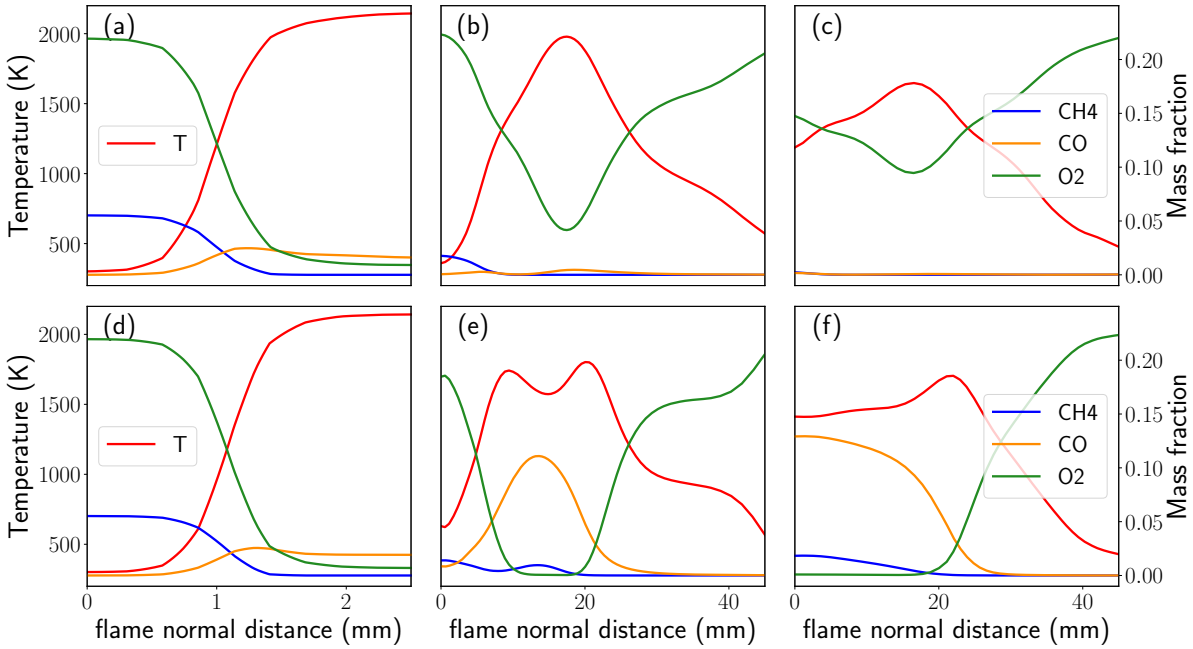

Figure 9: Time-averaged line plots of gas temperature and major species mass fractions along the flame normal direction. (a)-(c): pure pilot flame at x/d =0.57, 7.59, 16.46; (d)-(f): coal flame at x/d =0.57, 7.59, 16.46. The three downstream positions correspond to the typical premixed flame, double flame and typical diffusion flame regions shown in Fig. 8.

The existence of multi-mode combustion is confirmed by Fig. 10 which shows instantaneous scatter plots of gas temperature and major species mass fractions in (volatile) mixture fraction space for the coal flame. At $x/d = 7.59$ two distinct branches of the reacting

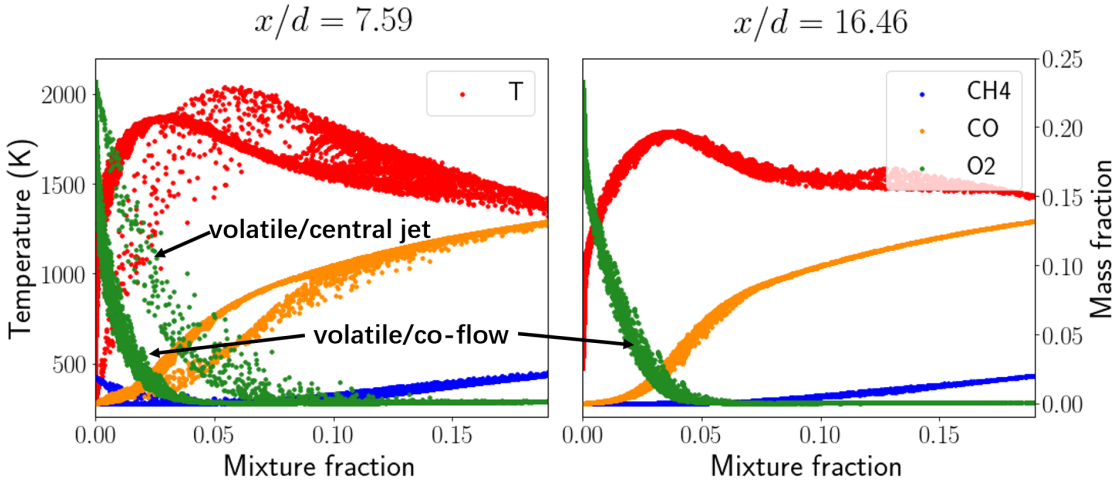

Figure 10: Instantaneous scatter plots of gas temperature and major species mass fractions vs. volatile mixture fraction at $x/d = 7.59$ (left) and $x/d = 16.46$ (right) for the coal flame.

scalars can be identified, which can be associated with volatile/co-flow and volatile/central jet mixing, respectively. Further downstream at $x/d = 16.46$ the branch associated with the mixing of the volatiles with the central jet has vanished and only the volatile/co-flow flame remains.

Particle dynamics

The flame structure can also be analysed from a particle perspective. The properties of the coal particles including diameter, particle temperature, volatile mass fraction retained within the particles and devolatilisation rate are plotted as a function of the radial coordinate at various downstream locations in Fig. 11 and two cases are compared. For all results of the coal flame discussed up to the present section a Rosin-Rammler size distribution has been assumed for particle injection at the inlet patch (blue circles in Fig. 11). To illustrate the effect that the assumption of a constant particle size at injection would have, the red triangles in Fig. 11 show data from an additional simulation where an equivalent uniform particle diameter was employed. Far upstream at $x/d = 0.63$, only the outer particles ($r/d > 0.5$) are heated and a small amount of volatiles is released. The temperature of the inner particles gradually increases with the downstream coordinate as mixing with the hot pilot and volatile flame proceeds. At $x/d = 7.59$, the outer particles have approximately reached the gas flame temperature and their devolatilisation process has finished, while considerable heat-up and pyrolysis occurs at intermediate radii and a small number of particles close to the axis ($r/d < 0.1$) still remains to be heated. The particle diameter data at $x/d = 7.59$ for the uniform case shows a decrease of d_p for $r/d > 0.5$, where pyrolysis occurs. However, this shrinking effect due to devolatilisation is small, because the volatile matter contributes only around 55% of the total mass, cf. Tab.1. Far downstream at $x/d = 16.46$, the volatile matter has been completely released and most of the particles are hot. The final row of Fig. 11 shows the devolatilisation rates for the Rosin-Rammler case only and particles are coloured according to their diameter d_p. Smaller particles are heated faster than larger particles,

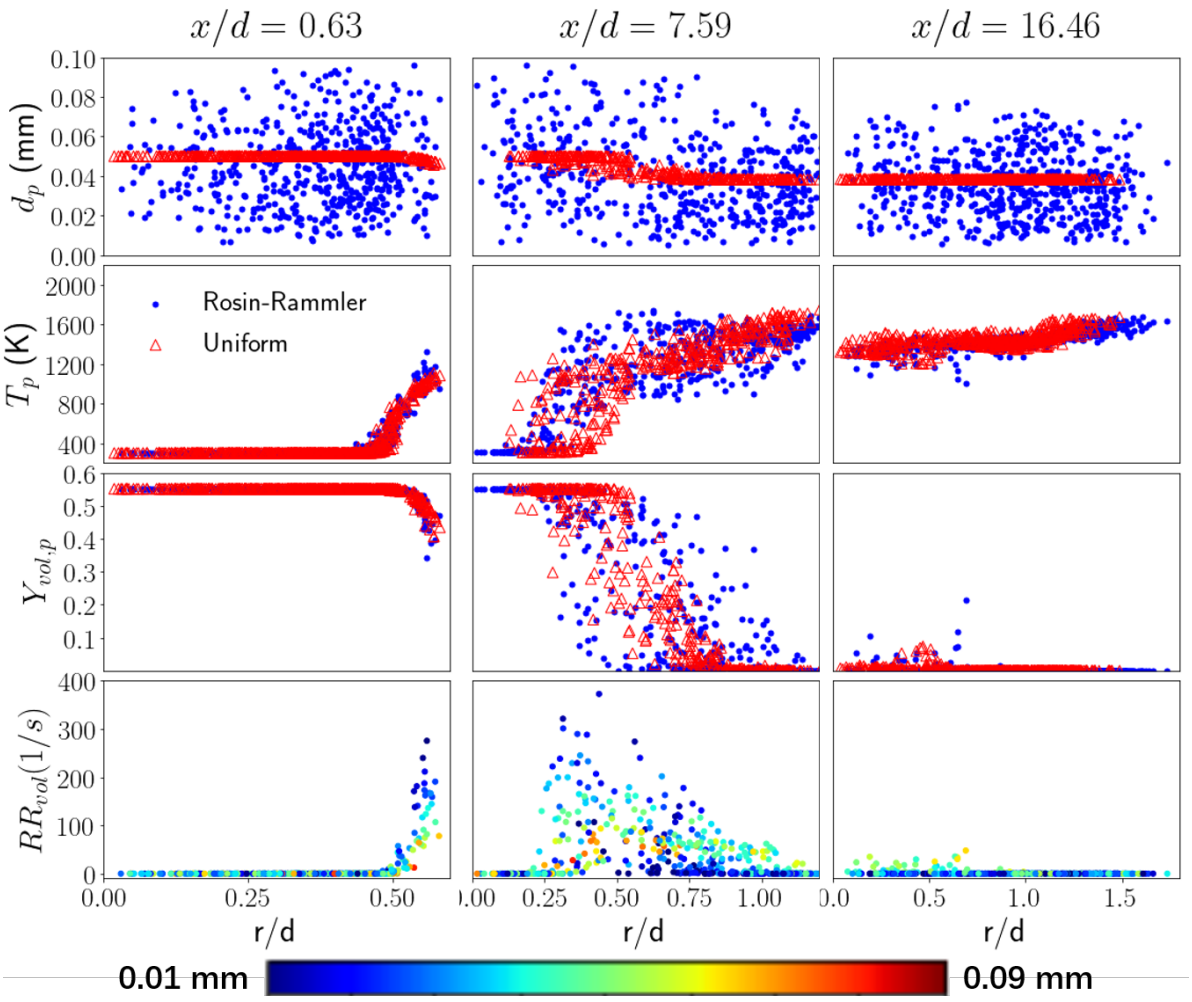

Figure 11: Top three rows: Radial distributions of the coal particle diameter d_p, particle temperature T_p and volatile mass fraction inside the coal particles $Y_{vol,p}$ at axial locations $x/d = 0.63$, $x/d = 7.59$ and $x/d = 16.46$ (left to right). Red triangles: uniform particle size, blue circles: Rosin-Rammler particle size distribution. Bottom row: Radial distribution of the devolatilisation rate RR_{vol} for the Rosin-Rammler case only, with the colourbar referring to particle diameter.

such that small particles devolatilise earlier. However, since with the employed single rate pyrolysis kinetics the devolatilisation rate is proportional to the mass of volatiles retained inside the coal particles, Eq. (16), intermediate size particles that contain considerably more volatile mass than small particles show comparable devolatilisation rates, whereas the lowest release rates are found for very large particles. Comparing the results from the Rosin-Rammler distribution to the uniform particle size in Fig. 11, overall only small differences

can be observed, which mainly affect $Y_{vol,p}$ in the far downstream region. This result is most likely due to the limited range of particle sizes which could be tested here, because of limitations related to the employed Euler-Lagrange framework, cf. modelling section.

As already discussed in the context of Fig. 6 the experimental snapshot suggests that the coal particles burn near the edge of central jet and that single particle combustion dominates over group combustion. According to the DNS study by Tufano et al. [7,44] the particle combustion mode can be identified by the ratio of the particle distance L_x to the particle diameter d_p, where small ratios of L_x/d_p indicate group combustion, whereas large ratios imply single particle burning. For a range of particle Reynolds numbers $2 < Re_p < 8$, the DNS identified ratios $L_x/d_p < 30$ as group combustion, while $L_x/d_p > 30$ resulted in single particle combustion. In the present FPV-LES calculations, the average particle Reynolds number Re_p is 6.4, so we consider the threshold $L_x/d_p = 30$ as valid for distinguishing between the modes. The coal particles from FPV-LES are sampled according to their axial and radial location, and the mean distance between neighbouring particles is calculated. The contours of the distance-to-diameter ratio L_x/d_p from the two models for initial particle size distribution are shown in Fig. 12, where the white lines indicate $L_x/d_p = 30$. As ex-

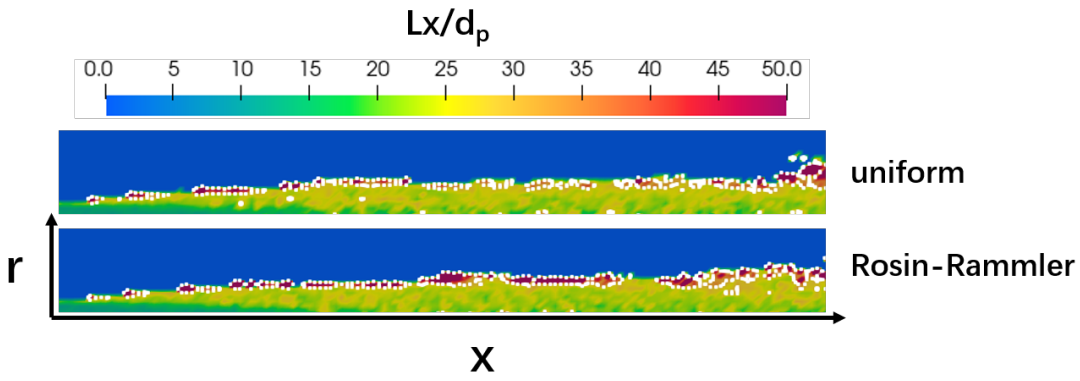

Figure 12: Contour plot of the ratio of inter-particle distance to particle diameter L_x/d_p, uniform particle size (top), Rosin-Rammler size distribution (bottom). The white lines indicate the region where $L_x/d_p = 30$. In the outer blue region no particles exist.

pected L_x/d_p increases with both the radial (strongly) and axial (weakly) coordinate. The

region with $L_x/d_p = 30$ lies near the edge of the central jet far upstream and shifts to higher radii with downstream distance. It separates the inner region with small values of L_x/d_p (group combustion) from the outer region with large particle spacings (i.e. individual particle combustion or no particles at all). The effect of the assumption on the particle size distribution is small, with the Rosin-Rammler model resulting in a somewhat broader region where $L_x/d_p = 30$. Overall, this simple analysis of the particle combustion mode seems to very well capture the experimental observation of the outer flame appearance being dominated by streaks of individually burning particles, cf. Fig. 6.

Conclusions

A multi-stream flamelet progress variable method coupled with large eddy simulation (FPV-LES) has been used to study coal combustion in the laboratory-scale, gas-assisted Cambridge Coal Burner within configuration CCB1. Three cases, namely non-reacting flow, pure pilot flame and pulverised coal combustion are simulated. The simulated velocity profiles are compared with the experimental evidence and despite some deviations in the upstream pilot region the overall agreement is considered acceptable. The simulations show that the effect of particle combustion in the upstream measurement region is very small for the coal flame, such that the velocities from both experiment and simulation for the pure pilot and coal flame are similar.

A thorough analysis of gas-assisted coal combustion and the contribution of the pilot flame is conducted based on the FPV-LES data for the pure pilot and coal case. The flame structure is found to undergo a transformation with downstream distance, where a typical premixed flame dominated by the pilot is found far upstream, followed by a double flame at intermediate locations and a typical non-premixed volatile flame far downstream. Two different inlet conditions for the particle size distribution are tested, and the results show that within the tested range the assumption of a constant particle diameter would only mildly

affect the results. Particle distance analysis is used to distinguish the modes of particle combustion. Consistent with the experimental observation, the observable particles at the outer side of the flame are found to be in a single particle combustion mode, whereas the inner particles tend to burn in groups. This study provides the first evaluation of pure pilot versus coal combustion in the complex CCB1 flame and advances our knowledge of modelling gas-assisted coal combustion by means of FPV-LES.

Acknowledgement

Support from the Natural Science Foundation of China (Grant No. 91441120) and the Center for Combustion Energy at Tsinghua University is gratefully acknowledged. The simulations were performed on ARCHER, funded under the EPSRC project "UK Consortium on Mesoscale Engineering Sciences (UKCOMES)" (Grant No. EP/R029598/1). This work was supported by the Deutsche Forschungsgemeinschaft (DFG, German Research Foundation) - projects 238057103 and 215035359 - TRR 129. We gratefully thank Tien Duc Luu for his help with radiation modelling.

References

(1) Nikrityuk, P. A.; Gräbner, M.; Kestel, M.; Meyer, B. Numerical study of the influence of heterogeneous kinetics on the carbon consumption by oxidation of a single coal particle. Fuel **2013**, 114, 88–98.

(2) Vascellari, M.; Tufano, G.; Stein, O. T.; Kronenburg, A.; Kempf, A. M.; Scholtissek, A.; Hasse, C. A flamelet/progress variable approach for modeling coal particle ignition. Fuel **2017**, 201, 29–38.

(3) Farazi, S.; Sadr, M.; Kang, S.; Schiemann, M.; Vorobiev, N.; Scherer, V.; Pitsch, H.

Resolved simulations of single char particle combustion in a laminar flow field. Fuel **2017**, 201, 15 – 28.

(4) Tufano, G.; Stein, O. T.; Kronenburg, A.; Gentile, G.; Stagni, A.; Frassoldati, A.; Faravelli, T.; Kempf, A.; Vascellari, M.; Hasse, C. Fully-resolved simulations of coal particle combustion using a detailed multi-step approach for heterogeneous kinetics. Fuel **2019**, 240, 75–83.

(5) Liu, X. J.; Li, L. Numerical studies on the combustion properties of char particle clusters. International Journal of Heat and Mass Transfer **2009**, 52, 4785–4795.

(6) Sayadi, T.; Farazi, S.; Kang, S.; Pitsch, H. Transient multiple particle simulations of char particle combustion. Fuel **2017**, 199, 289–298.

(7) Tufano, G.; Stein, O. T.; Wang, B.; Kronenburg, A.; Rieth, M.; Kempf, A. Coal particle volatile combustion and flame interaction. Part I: Characterization of transient and group effects. Fuel **2018**, 229, 262–269.

(8) Luo, K.; Wang, H.; Fan, J.; Yi, F. Direct Numerical Simulation of Pulverized Coal Combustion in a Hot Vitiated Co-flow. Energy & Fuels **2012**, 26, 6128–6136.

(9) Brosh, T.; Patel, D.; Wacks, D.; Chakraborty, N. Numerical investigation of localised forced ignition of pulverised coal particle-laden mixtures: A Direct Numerical Simulation (DNS) analysis. Fuel **2015**, 145, 50 – 62.

(10) Krüger, J.; Haugen, N. E. L.; Lovas, T. Correlation effects between turbulence and the conversion rate of pulverized char particles. Combustion and Flame **2017**, 185, 160 – 172.

(11) Muto, M.; Yuasa, K.; Kurose, R. Numerical simulation of ignition in pulverized coal combustion with detailed chemical reaction mechanism. Fuel **2017**, 190, 136 – 144.

(12) Wan, K.; Vervisch, L.; Xia, J.; Domingo, P.; Wang, Z.; Liu, Y.; Cen, K. Alkali metal emissions in an early-stage pulverized-coal flame: DNS analysis of reacting layers and chemistry tabulation. Proceedings of the Combustion Institute **2019**, 37, 2791 – 2799.

(13) Rieth, M.; Kempf, A. M.; Kronenburg, A.; Stein, O. T. Carrier-phase DNS of pulverized coal particle ignition and volatile burning in a turbulent mixing layer. Fuel **2018**, 212, 364 – 374.

(14) Kurose, R.; Watanabe, H.; Makino, H. Numerical simulations of pulverized coal combustion. KONA Powder and Particle Journal **2009**, 27, 144–156.

(15) Edge, P.; Gubba, S.; Ma, L.; Porter, R.; Pourkashanian, M.; Williams, A. LES modelling of air and oxy-fuel pulverised coal combustion - impact on flame properties. Proceedings of the Combustion Institute **2011**, 33, 2709–2716.

(16) Stein, O. T.; Olenik, G.; Kronenburg, A.; Marincola, F. C.; Franchetti, B.; Kempf, A.; Ghiani, M.; Vascellari, M.; Hasse, C. Towards comprehensive coal combustion modelling for LES. Flow, Turbulence and Combustion **2013**, 90, 859–884.

(17) Yamamoto, K.; Murota, T.; Okazaki, T.; Taniguchi, M. Large eddy simulation of a pulverized coal jet flame ignited by a preheated gas flow. Proceedings of the Combustion Institute **2011**, 33, 1771 – 1778.

(18) Franchetti, B.; Marincola, F. C.; Navarro-Martinez, S.; Kempf, A. Large Eddy simulation of a pulverised coal jet flame. Proceedings of the Combustion Institute **2013**, 34, 2419 – 2426.

(19) Olenik, G.; Stein, O. T.; Kronenburg, A. LES of swirl-stabilised pulverised coal combustion in IFRF furnace No. 1. Proceedings of the Combustion Institute **2015**, 35, 2819 – 2828.

(20) Pierce, C. D.; Moin, P. Progress-variable approach for large-eddy simulation of non-premixed turbulent combustion. Journal of Fluid Mechanics **2004**, 504, 73–97.

(21) Watanabe, J.; Yamamoto, K. Flamelet model for pulverized coal combustion. Proceedings of the Combustion Institute **2015**, 35, 2315–2322.

(22) Vascellari, M.; Xu, H.; Hasse, C. Flamelet modeling of coal particle ignition. Proceedings of the Combustion Institute **2013**, 34, 2445–2452.

(23) Messig, D.; Vascellari, M.; Hasse, C. Flame structure analysis and flamelet progress variable modelling of strained coal flames. Combustion Theory and Modelling **2017**, 21, 700–721.

(24) Wen, X.; Luo, K.; Wang, H.; Luo, Y.; Fan, J. Analysis of pulverized coal flame stabilized in a 3D laminar counterflow. Combustion and Flame **2018**, 189, 106–125.

(25) Watanabe, J.; Okazaki, T.; Yamamoto, K.; Kuramashi, K.; Baba, A. Large-eddy simulation of pulverized coal combustion using flamelet model. Proceedings of the Combustion Institute **2017**, 36, 2155–2163.

(26) Rieth, M.; Proch, F.; Rabaçal, M.; Franchetti, B.; Marincola, F. C.; Kempf, A. Flamelet LES of a semi-industrial pulverized coal furnace. Combustion and Flame **2016**, 173, 39–56.

(27) Rieth, M.; Clements, A.; Rabaçal, M.; Proch, F.; Stein, O. T.; Kempf, A. Flamelet LES modeling of coal combustion with detailed devolatilization by directly coupled CPD. Proceedings of the Combustion Institute **2017**, 36, 2181–2189.

(28) Knappstein, R.; Künne, G.; Meier, T.; Sadiki, A.; Janicka, J. Evaluation of coal particle volatiles reaction by using detailed kinetics and FGM tabulated chemistry. Fuel **2017**, 201, 39 – 52.

(29) Knappstein, R.; Künne, G.; Becker, L. G.; di Mare, F.; Sadiki, A.; Dreizler, A.; Janicka, J. Large Eddy Simulation of a Novel Gas-Assisted Coal Combustion Chamber. Flow, Turbulence and Combustion **2018**, 101, 895–926.

(30) Molina, A.; Shaddix, C. R. Ignition and devolatilization of pulverized bituminous coal particles during oxygen/carbon dioxide coal combustion. Proceedings of the Combustion Institute **2007**, 31, 1905–1912.

(31) Toporov, D.; Bocian, P.; Heil, P.; Kellermann, A.; Stadler, H.; Tschunko, S.; Förster, M.; Kneer, R. Detailed investigation of a pulverized fuel swirl flame in CO_2/O_2 atmosphere. Combust. Flame **2008**, 155, 605–618.

(32) Maffei, T.; Khatami, R.; Pierucci, S.; Faravelli, T.; Ranzi, E.; Levendis, Y. A. Experimental and modeling study of single coal particle combustion in O_2/N_2 and Oxy-fuel (O_2/CO_2) atmospheres. Combust. Flame **2013**, 160, 2559–2572.

(33) Vorobiev, N.; Geier, M.; Schiemann, M.; Scherer, V. Experimentation for char combustion kinetics measurements: Bias from char preparation. Fuel Proces. Technol. **2016**, 151, 155 – 165.

(34) C. Hasse et al., Workshop on Coal and Biomass Conversion (CBC). http://www.cbc.uni-due.de, 2020; Accessed: 2020-01-23.

(35) Hwang, S. M.; Kurose, R.; Akamatsu, F.; Tsuji, H.; Makino, H.; Katsuki, M. Application of optical diagnostics techniques to a laboratory-scale turbulent pulverized coal flame. Energy & Fuels **2005**, 19, 382–392.

(36) Hwang, S. M.; Kurose, R.; Akamatsu, F.; Tsuji, H.; Makino, H.; Katsuki, M. Observation of detailed structure of turbulent pulverized-coal flame by optical measurement. JSME International Journal Series B Fluids and Thermal Engineering **2006**, 49, 1316–1327.

(37) Becker, L. G.; Kosaka, H.; Böhm, B.; Doost, S.; Knappstein, R.; Habermehl, M.; Kneer, R.; Janicka, J.; Dreizler, A. Experimental investigation of flame stabilization inside the quarl of an oxyfuel swirl burner. Fuel **2017**, 201, 124 – 135.

(38) Balusamy, S.; Schmidt, A.; Hochgreb, S. Flow field measurements of pulverized coal combustion using optical diagnostic techniques. Experiments in Fluids **2013**, 54, 1534.

(39) Balusamy, S.; Kamal, M. M.; Lowe, S. M.; Tian, B.; Gao, Y.; Hochgreb, S. Laser diagnostics of pulverized coal combustion in O_2/N_2 and O_2/CO_2 conditions: velocity and scalar field measurements. Experiments in Fluids **2015**, 56, 108.

(40) Muto, M.; Watanabe, H.; Kurose, R.; Komori, S.; Balusamy, S.; Hochgreb, S. Large-eddy simulation of pulverized coal jet flame - Effect of oxygen concentration on NO_x formation. Fuel **2015**, 142, 152–163.

(41) Smagorinsky, J. General circulation experiments with the primitive equations. Monthly Weather Review **1963**, 91, 99–164.

(42) Kuo, K. K. Principles of combustion; Wiley & Sons, 2005.

(43) Tufano, G.; Stein, O. T.; Kronenburg, A.; Frassoldati, A.; Faravelli, T.; Deng, L.; Kempf, A.; Vascellari, M.; Hasse, C. Resolved flow simulation of pulverized coal particle devolatilization and ignition in air- and O_2/CO_2-atmospheres. Fuel **2016**, 186, 285–292.

(44) Tufano, G.; Stein, O. T.; Wang, B.; Kronenburg, A.; Rieth, M.; Kempf, A. Coal particle volatile combustion and flame interaction. Part II: Effects of particle Reynolds number and turbulence. Fuel **2018**, 234, 723–731.

(45) Ranzi, E.; Frassoldati, A.; Granata, S.; Faravelli, T. Wide-range kinetic modeling study of the pyrolysis, partial oxidation, and combustion of heavy n-alkanes. Industrial & engineering chemistry research **2005**, 44, 5170–5183.

(46) Muto, M.; Tanno, K.; Kurose, R. A DNS study on effect of coal particle swelling due to devolatilization on pulverized coal jet flame. Fuel **2016**, 184, 749 – 752.

(47) Grant, D.; Pugmire, R.; Fletcher, T.; Kerstein, A. Chemical Model of Coal Devolatilization Using Percolation Lattice Statistics. Energy & Fuels **1989**, 3, 175–186.

(48) Cheng, P. Two-dimensional radiating gas flow by a moment method. AIAA Journal **1964**, 2, 1662–1664.

(49) Barlow, R.; Karpetis, A.; Frank, J.; Chen, J.-Y. Scalar profiles and NO formation in laminar opposed-flow partially premixed methane/air flames. Combustion and Flame **2001**, 127, 2102 – 2118.

(50) Müller, H.; Ferraro, F.; Pfitzner, M. Implementation of a Steady Laminar Flamelet Model for non-premixed combustion in LES and RANS simulations. 8th Internat. OpenFOAM Workshop, Jeju, Korea **2013**,

(51) Wen, X.; Wang, H.; Luo, Y.; Luo, K.; Fan, J. Evaluation of flamelet/progress variable model for laminar pulverized coal combustion. Physics of Fluids **2017**, 29, 083607.

(52) Xing, J.; Luo, K.; Chen, Y.; Stein, O. T.; Kronenburg, A.; Luo, K. H.; Hasse, C.; Fan, J. Large eddy simulation of Cambridge bluff-body coal (CCB2) flames with a flamelet progress variable model. 38^{th} International Symposium on Combustion (accepted for presentation).

(53) Chen, Y.; Stein, O. T.; Kronenburg, A.; Vascellari, M.; Hasse, C.; Luo, H., Kai Flamelet progress variable modelling of pulverised coal devolatilisation and burning in opposed jets. Conference on Modelling Fluid Flow (CMFF'18), The 17th International Conference on Fluid Flow Technologies Budapest, Hungary, September 4-7, 2018. 2018.